



AFRL-RX-WP-TP-2010-4137

**DERIVING THE GRAIN BOUNDARY CHARACTER
DISTRIBUTION AND RELATIVE ENERGIES FROM
THREE DIMENSIONAL EBSD DATA (PREPRINT)**

**Gregory S. Rohrer, Jia Li, Sukbin Lee, Anthony D. Rollett, Michael Groeber,
and Michael D. Uchic**

Metals Branch

Metals, Ceramics & NDE Division

APRIL 2010

Approved for public release; distribution unlimited.

See additional restrictions described on inside pages

STINFO COPY

**AIR FORCE RESEARCH LABORATORY
MATERIALS AND MANUFACTURING DIRECTORATE
WRIGHT-PATTERSON AIR FORCE BASE, OH 45433-7750
AIR FORCE MATERIEL COMMAND
UNITED STATES AIR FORCE**

REPORT DOCUMENTATION PAGE				Form Approved OMB No. 0704-0188	
<p>The public reporting burden for this collection of information is estimated to average 1 hour per response, including the time for reviewing instructions, searching existing data sources, gathering and maintaining the data needed, and completing and reviewing the collection of information. Send comments regarding this burden estimate or any other aspect of this collection of information, including suggestions for reducing this burden, to Department of Defense, Washington Headquarters Services, Directorate for Information Operations and Reports (0704-0188), 1215 Jefferson Davis Highway, Suite 1204, Arlington, VA 22202-4302. Respondents should be aware that notwithstanding any other provision of law, no person shall be subject to any penalty for failing to comply with a collection of information if it does not display a currently valid OMB control number. PLEASE DO NOT RETURN YOUR FORM TO THE ABOVE ADDRESS.</p>					
1. REPORT DATE (DD-MM-YY) April 2010		2. REPORT TYPE Journal Article Preprint		3. DATES COVERED (From - To) 01 April 2010 – 01 April 2010	
4. TITLE AND SUBTITLE DERIVING THE GRAIN BOUNDARY CHARACTER DISTRIBUTION AND RELATIVE ENERGIES FROM THREE DIMENSIONAL EBSD DATA (PREPRINT)				5a. CONTRACT NUMBER In-house	
				5b. GRANT NUMBER	
				5c. PROGRAM ELEMENT NUMBER 62102F	
6. AUTHOR(S) Gregory S. Rohrer, Jia Li, Sukbin Lee, Anthony D. Rollett, Michael Groeber, and Michael D. Uchic				5d. PROJECT NUMBER 4347	
				5e. TASK NUMBER RG	
				5f. WORK UNIT NUMBER M02R1000	
7. PERFORMING ORGANIZATION NAME(S) AND ADDRESS(ES) Metals Branch (AFRL/RXLM) Metals, Ceramics & NDE Division Air Force Research Laboratory, Materials and Manufacturing Directorate Wright-Patterson Air Force Base, OH 45433-7750 Air Force Materiel Command, United States Air Force				8. PERFORMING ORGANIZATION REPORT NUMBER AFRL-RX-WP-TP-2010-4137	
9. SPONSORING/MONITORING AGENCY NAME(S) AND ADDRESS(ES) Air Force Research Laboratory Materials and Manufacturing Directorate Wright-Patterson Air Force Base, OH 45433-7750 Air Force Materiel Command United States Air Force				10. SPONSORING/MONITORING AGENCY ACRONYM(S) AFRL/RXLMD	
				11. SPONSORING/MONITORING AGENCY REPORT NUMBER(S) AFRL-RX-WP-TP-2010-4137	
12. DISTRIBUTION/AVAILABILITY STATEMENT Approved for public release; distribution unlimited.					
13. SUPPLEMENTARY NOTES Journal article submitted to <i>Materials Science and Technology</i> . PAO Case Number: 88ABW-2009-2744; Clearance Date: 22 Jun 2009. Paper contains color.					
14. ABSTRACT Three-dimensional electron backscattered diffraction data from a nickel-base super alloy has been analyzed to measure the geometric arrangement of grain boundary planes at triple junctions. This information has been used to calculate the grain boundary character distribution (GBCD) and the grain boundary energy distribution (GBED). The twin content from the three-dimensional GBCD calculation compares favorably with the twin content estimated by stereology. Important factors in the analysis are the alignment of the parallel layers, the ratio of the vertical to horizontal spacing, and the discretization of the domain of grain boundary types. The results show that the GBCD and GBED are inversely correlated.					
15. SUBJECT TERMS grain boundary character distribution (GBCD), grain boundary energy distribution (GBED)					
16. SECURITY CLASSIFICATION OF:			17. LIMITATION OF ABSTRACT: SAR	18. NUMBER OF PAGES 34	19a. NAME OF RESPONSIBLE PERSON (Monitor) Christopher F. Woodward 19b. TELEPHONE NUMBER (Include Area Code) N/A
a. REPORT Unclassified	b. ABSTRACT Unclassified	c. THIS PAGE Unclassified			

Deriving the grain boundary character distribution and relative energies from three dimensional EBSD data

Gregory S. Rohrer, Jia Li, Sukbin Lee, Anthony D. Rollett, Michael Groeber, Michael D. Uchic.

Abstract

Three-dimensional electron backscattered diffraction data from a nickel-base super alloy has been analyzed to measure the geometric arrangement of grain boundary planes at triple junctions. This information has been used to calculate the grain boundary character distribution (GBCD) and the grain boundary energy distribution (GBED). The twin content from the three-dimensional GBCD calculation compares favorably with the twin content estimated by stereology. Important factors in the analysis are the alignment of the parallel layers, the ratio of the vertical to horizontal spacing, and the discretization of the domain of grain boundary types. The results show that the GBCD and GBED are inversely correlated.

Introduction

Microstructures have traditionally been characterized on the basis of observations of two-dimensional plane sections. Recognizing that microstructures are actually comprised of three-dimensional objects, stereological techniques have been developed to extract three-dimensional information from two-dimensional observations. However, such information is always constrained by certain assumptions about the distribution, shape, and orientations of the microstructural components. Furthermore, stereological analysis produces statistical information about groups of objects instead of quantities that can be associated with specific objects.

The focus of the current paper is on determining the orientations of grain boundary planes and the geometries of triple lines within polycrystalline structures. In the past, serial sectioning by polishing or milling, combined with electron backscatter diffraction (EBSD) mapping has been used to determine grain boundary

plane orientations [1-5]. However, the limited use of this technique over the years is evidence of the method's difficulty. Stereology, on the other hand, has been applied extensively [6-13]. However, this provides information about the distributions of planes, not specific planes or the configuration of the planes at triple lines.

The development of the dual beam focused ion beam (DB-FIB) scanning electron microscope (SEM) makes it possible to automate the serial sectioning and EBSD mapping processes. An orientation map is measured on a surface, a thin section is removed by ion milling, and then the process is repeated on a parallel layer. The possibility of recording parallel EBSD maps and reconstructing the grain shapes in three-dimensions has already been demonstrated [14-19]. The results show that it is possible to measure several characteristics of the grain level microstructure, including the distribution of grain sizes, shapes, and orientations.

Methods have also been developed to compute the grain boundary character distribution (GBCD) and, from the geometries of the triple lines, the relative grain boundary energy distribution (GBED) from three-dimensional EBSD data [20, 21]. The purposes of the current paper are to describe in detail the processes used to evaluate the GBCD and to demonstrate the efficacy of the procedures. The procedures are applied to data from a Ni-base super alloy with a high degree of twinning; the twins act as an internal standard against which our results can be compared. Using the twins as a guide, we find that appropriate discretization and layer-to-layer alignment are the most important factors in determining accurate interface geometry. The resulting GBCD and GBED are presented as a demonstration of the method.

Methods

The procedures for collection of the data have already been described in detail [14,15,18,19]. Here, new information (the GBCD and GBED) are derived from this same data. The sample is a powder-processed nickel-base superalloy (IN100) with a mean grain diameter of about 3 μm . The sample is dual phase, containing γ

and coherent γ' precipitates. However, the phases were not resolved by the EBSD study so each grain is considered to be single phase.

The data consists of 170 parallel EBSD maps. Each map is 45 x 45 microns and separated by 0.2 microns. The analysis steps we use can be divided into two groups: those that can be carried out using commercially available 3-D OIM visualization software (EDAX, Mahwah, NJ), and those for which we use software developed at Carnegie Mellon. For example, in the initial steps, the data was cropped to remove unindexed points at the periphery of each image. The EBSD data was cleaned using two iterations of grain dilation in the OIM software with a minimum grain size of 10 pixels. This procedure considers any grouping of less than 10 pixels, with disorientations of less than 5° , to be insufficient to define a single grain and assigns their orientation to match the orientation of an adjacent grain. A single average orientation was assigned to each grain, with an individual grain being defined as a set of pixels whose disorientations lie within 5° of one another.

The next step is to align the layers so that they have a common lateral reference frame. This is necessary because of misalignments introduced by the sample rotations that take place between each milling and EBSD mapping step. At this stage, the data were aligned on a fixed grid. This will be referred to as primary alignment. The OIM software can perform the primary alignment by maximizing the cross-correlation between the three different color channels in the orientation image map. A procedure that minimizes the disorientation between corresponding voxels on adjacent layers was also developed and an image of a portion of the data aligned in this way is shown in Fig. 1 [22]. Both methods preserve a fixed grid for the data and produce comparable results.

The next step is to approximate the grain boundaries on each layer with straight line segments. Again, this can be accomplished with the OIM software as long as the data are on a hexagonal grid. The data analyzed here was acquired on a square grid so it was converted to a hexagonal grid using the freely available program, OIMTools [23]. With the orientations on a hexagonal grid, the OIM

software was used to determine grain boundary line segments approximating the true positions for the boundaries according to a procedure described in ref. [24]. For the line segment extraction, a maximum deviation of two pixels was permitted between the actual boundary position and the reconstructed line segment. An example of the reconstructed grain boundary line segments, superimposed on the EBSD map, is shown in Fig. 2. While this makes the boundaries appear polygonal, it can also be seen that the reconstructed segments are smooth approximations of the true boundary positions. For each layer, the OIM software produces a list of line segments that specifies, among other things, the Euler angles for the grains on either side of the line and the initial and final coordinates. The remainder of the analysis is carried out on these lists of line segments using software developed at Carnegie Mellon.

The first step of calculating the GBCD and GBED is to locate each triple junction. On each layer, the list of line segments is searched to identify all groups of three line segments whose end points share an identical coordinate. These triplets are then saved. After all of the triple junctions are identified on each layer, they are compared. To find triple junctions on adjacent layer that are connected by a triple line, the lateral coordinates of each triple junction are compared. For the five junctions on an adjacent layer that have the closest lateral coordinates, the three crystal orientations on the first layer are compared to the three on the second layer. If the disorientations between the crystals on the top layer and the bottom layer are all less than 5° , a triple line is assumed to connect the two triple junctions between the layers. Because some topological changes occur between the section planes, only a fraction of all of the triple junctions can be matched. Typically, 70 % to 90 % of the junctions on each layer are matched to a junction on an adjacent layer.

The triple junction is now characterized by three vectors on each layer and a vector connecting them along the triple line, as illustrated in Fig 3. The data are sorted so that the vectors are listed in counter clockwise order around the line. The grain boundary normal orientation is now determined by the cross product of \mathbf{l} and \mathbf{v}_i . The area of the boundary plane is one half of the magnitude of the cross product. The three vectors on the top layer produce three normal vectors and the three on

the lower layer produce three more. The area of each of these triangles is added to the appropriate discrete grain boundary type, determined by its misorientation and boundary normal. The five dimensional space of grain boundary types is discretized as described earlier [25]. The sum of these areas make up the GBCD.

In an equiaxed microstructure, one expects the orientations of the triple lines to be randomly distributed about the sample normal direction. However, when the triple line directions are examined, their distribution is typically biased. For example, Fig. 4 shows the directions of 118 triple lines between the second and third layer of the data. The circles represent the positions of the lines and because they are on a discrete grid, many of the points overlap. The lines clearly are biased in the positive y direction. Assuming this is due to an alignment error, a rigid shift can be applied to the coordinates of the third layer, so that the average triple line direction is perpendicular to the surface. This rigid shift is referred to as the secondary alignment procedure. The shifted data are represented by the red squares and the shift is shown by the black arrow. The shifts applied to all 170 layers are shown in Fig. 5. The displacements in the vertical (y) direction are larger than the horizontal (x) component. This is probably because the sample is tilted by 70° with respect to the beam so that positioning errors in the y-direction are magnified by a factor of about 3 ($1/\cos(70)$). Note that the secondary alignment moves the data off of the fixed grid. To test the efficacy of this procedure, data with and without the secondary alignment will be compared in the results section.

Because we connect triple lines on adjacent layers, and the layer spacing is the same as the in-plane spacing, the triple lines are constrained to adopt discrete orientations in the sample reference frame, as depicted schematically in Fig. 6. To test the effect of this discretization, the procedures described above were repeated, except triple junctions were matched from every other layer. Increasing the ratio of the vertical to horizontal spacing from 1:1 to 2:1 and also decreasing the minimum angular separation of the discrete directions.

The grain boundary energies were calculated using the capillarity vector method, developed by Morawiec [26]. The capillarity vector reconstruction method is similar to many other interface energy measurements in that the experimental

observable is the interfacial geometry; the energy is computed from the geometry using an expression for interfacial equilibrium. In this case, the equilibrium at the triple line is described by the Herring [27] equation. Therefore, the key assumption underpinning this and previous measurements of relative grain boundary energies is that the interfacial junctions are in local thermodynamic equilibrium.

The capillary vector reconstruction method was described in detail in ref. [26] and first applied to real data in ref. [28]. The current energy calculation was carried out in exactly the same way, using the same computer programs that were used in refs. [26] and [28]. Here, only a brief summary of the method is presented. The Herring [27] condition, when expressed in terms of capillarity vectors [29,30], is:

$$(\xi^1 + \xi^2 + \xi^3) \times \mathbf{l} = 0 \quad (1)$$

where ξ^1 , ξ^2 , and ξ^3 are the capillarity vectors associated with the three grain boundaries and \mathbf{l} is the triple line. Each capillarity vector has a component perpendicular to the grain boundary whose magnitude is equal to the relative grain boundary energy. Each capillarity vector also has a component tangent to the boundary whose magnitude is the differential of the energy with respect to a right-handed rotation about \mathbf{l} . The normal and tangent vectors for 15,000 grain boundary triple junctions have been measured (using a vertical-to-horizontal spacing ratio of 2:1) and eq. 1 can be applied to each junction. The unknowns, which are the magnitudes of the capillarity vectors, are determined by an iterative procedure that finds the set of ξ that most nearly satisfy the 15,000 equilibrium equations. The final result was smoothed by replacing the value of ξ in each cell with the average of that vector and the vectors in the adjacent cells. The relative grain boundary energy is given by $\gamma = \xi \cdot \mathbf{n}$, where \mathbf{n} is the grain boundary normal. Previous calculations using simulated data based on model energy functions showed that the capillarity vector method reproduced all of the trends in the function, but did not quantitatively reproduce the depths of cusps [26, 28]. Based on these findings, it is

assumed that actual GBED is more anisotropic than the reconstructed distribution presented here.

Results

To test the efficacy of the reconstruction procedure, we can examine the GBCD at the $\Sigma 3$ misorientation, which is a 60° rotation about the $[111]$ axis. First, we compute the GBCD by an established stereological procedure [6]. The resulting distribution of grain boundary planes for the $\Sigma 3$ misorientation is shown in Fig. 7a. The results are plotted in stereographic project and are represented in multiples of a random distribution (MRD) units. MRD units are computed by dividing the total area of a given grain boundary type by the average area per boundary type. The large peak of 1100 MRD at the (111) orientation corresponds to the pure twist configuration which, in this case, is the coherent twin.

The distribution of grain boundary planes from the three-dimensional measurement, with a 1:1 ratio of the vertical-to-horizontal spacing and without secondary alignment, is shown in Fig. 7b. The peak of the distribution for the twin (240 MRD) is less than that determined stereologically and this suggests that the grain boundary plane orientations are not accurately determined. When the calculation is repeated with a 2:1 ratio of the vertical to horizontal spacing, the twin population increases to 390 MRD. When the calculation is repeated after the secondary alignment procedure (but a 1:1 ratio of the vertical-to-horizontal spacing), the twin population increases to 670 MRD. Finally, if the calculation is repeated using both the 2:1 ratio and the secondary alignment, the population increases to 1090 MRD, essentially identical to the stereologically determined population. The distribution of grain boundary planes for this calculation is shown in Fig. 7c.

It is possible to get a reliable estimate of the total fractional area of coherent twins within the microstructure by a second method [24]. For all boundary segments with the $\Sigma 3$ misorientation (within Brandon's [31] criterion), the orientation of the segment can be compared to the orientation of the ideal twin

plane. If the segment is within $\pm 10^\circ$ of the ideal orientation, it is assumed to be a coherent twin. Analyzing our data in this way, we find that twin boundaries make up 21.9 % of all of the grain boundary length observed on the plane sections. With a 10° discretization, there are approximately 6500 discrete grain boundary types. So, assuming all of the twins are classified as a single type, the distribution at this point should have a value of 1400 MRD. The computed values of approximately 1100 MRD differ by more than 20 % from this estimate.

One source of this deviation lies in an unfortunate choice of the discretization discretization of grain boundary types, which divides each angular range of 90° into 9 discrete categories [25]. The ideal Euler angles for the twin misorientation are $\phi_1=45^\circ$, $\Phi=70.5^\circ$, $\phi_2=45^\circ$. Because it is $\cos\Phi$ that is discretized, the limits of each bin occur at intervals of $1/9$. For the coherent twin, $\cos\Phi = 3/9$ and it therefore falls exactly on the border between bins. As a result, the population of the twin is split between multiple bins and always appears lower than expected. A simple way to change this to use a number other than $1/9$. For example, when we used $1/11$, the twin population increases to 3600 MRD (see Fig. 7d). In this discretization scheme, there are approximately 18000 distinct boundary types so we expect 3900 MRD at the twin orientation. The expectation and observation differ by less than 10 %, so we conclude that the calculations used to analyze the data and create the distribution are sufficiently accurate.

The finer discretization, however, has the potential to create other artifacts. With 11 bins per 90° , the same amount of data is distributed among almost three times as many bins, so it becomes sparse. Because roughly one quarter of all boundaries are $\Sigma 3$ type, this part of the distribution is sufficiently populated at this resolution. However, on average, less than 15 % of the boundary types have more than 10 observations. On the other hand, with 9 bins per 90° , well over half of the boundary types have more than 10 observations. Therefore, the remainder of the results will be presented from calculations discretized with 9 bins per 90° .

The distribution of grain boundary planes in the crystal reference frame is plotted in Fig. 8a. This distribution does not consider the grain boundary

misorientation. The minimum of the distribution occurs at [100] and the maximum occurs at [111]. The (111) plane is the closest packed and the habit plane for the twin, so it is presumed to have the lowest energy. This is confirmed by the result in Fig. 8b, which shows the relative energy of the grain boundary planes, in the crystal reference frame. The minimum energy occurs at the (111) orientation and the maximum at the (100) position. In other words, when the lattice misorientation is ignored, the grain boundary energy is inversely correlated to the population.

The GBED for the $\Sigma 3$ grain boundary is shown in Fig. 9. The minimum of the energy occurs at the position of the coherent twin where the population is maximized. As expected, the energy of the twin is the global minimum of the entire GBED (all misorientations) and the relative area of the twin is the global maximum of the GBCD.

The GBCDs and GBEDs for the $\Sigma 5$, $\Sigma 7$, and $\Sigma 9$ misorientations are compared in Fig. 10. The $\Sigma 5$ grain boundary occurs relatively infrequently; the populations are all less than 1 MRD. The distribution of grain boundary planes for the $\Sigma 7$ boundary shows a maximum (8 MRD) at the pure twist position and the grain boundary plane distribution for the $\Sigma 9$ boundary has a greater than random distribution for tilt grain boundaries (those in the [110] zone). There is a general correspondence between orientations of high population and low energy, and between low population and high energy. However, there are also notable exceptions. For example, the minimum energy configuration of the $\Sigma 9$ boundary occurs for the asymmetric tilt boundary $(-111)/(1-15)$, but the maximum population occurs near the position of the (1-14) symmetric tilt grain boundary.

To illustrate the average relationship between the grain boundary energy and population, the grain boundary energies were categorized into evenly spaced bins of width 0.1 a.u. and the average population and average energy of all of the boundaries in each bin was determined. The logarithms of the average populations are shown in Fig. 11. These data show that on average, the grain boundary population of a material is inversely correlated to the relative grain boundary energy.

Discussion

The results shown here demonstrate that to derive accurate grain boundary plane distributions, a secondary alignment procedure that moves the points from a fixed grid is necessary. The majority of the shifts are less than twice the spacing between the orientations ($0.2\ \mu\text{m}$) in the x-direction. In the y-direction, it is roughly three times this value. If the uncertainty in the x-direction is projected onto the sample plane tilted at 70° , it is expanded by a factor of approximately three. Without these alignments, the observed population is significantly lower than the expected value.

The results also suggest that increasing the vertical-to-horizontal spacing ratio leads to a more accurate distribution. The spacing between the vertical layers must clearly remain a small fraction of the average grain diameter (ideally, $\leq 1/10^{\text{th}}$), so this means that the spacing between the orientation data in the plane of the EBSD map should be decreased in comparison to the necessary layer spacing.

It is also apparent that the discretization of the space of grain boundary types influences the results. Those that fall on boundaries between the discrete bins have lower than expected populations and this happens for the $\Sigma 3$ boundary when there are 9 bins per 90° . When the space is discretized so that there are 11 bins per 90° , the observed population of $\Sigma 3$ boundaries is only 8 % less than the expected value. There are two possible sources for this remaining discrepancy. One is simply that the alignment is imperfect and/or there are other uncorrected distortions. For example, the spacing between layers might not be perfectly uniform or the misalignment may involve a rotation in addition to a translation. A second possibility is that the difference is an artifact of the way the two quantities are calculated. The estimate for the number of twins involves all line segments, while the GBCD calculation involves only those segments that meet at triple junctions. Segments of $\Sigma 3$ boundaries within grains and at the edges of images will not contribute to the GBCD calculation.

The GBCD of this Ni-base super alloy has some similarities to the distributions observed in other fcc metals including aluminum [7], brass [9] copper [12], stainless steel [10], and commercial purity Ni [12]. There are, however, a few distinctions. First, there is a relatively strong peak at the $\Sigma 7$ pure twist boundary formed by two (111) planes. Aluminum is the only one of the previously studied materials that showed a significant population of these boundaries [7]. Another main difference lies in the distribution of grain boundary plane orientations at the $\Sigma 9$ misorientation. The number of $\Sigma 9$ boundaries is relatively low and the (1-14) symmetric boundary is preferred. Once again, this characteristic is similar to aluminum [7]; the other fcc materials prefer asymmetric tilt boundaries [9,10,12].

Recently, the GBCD and GBED of a 99.999% pure Ni sample has been studied using the same methods [21]. Not surprisingly, many aspects of the distributions are similar. In both cases, the (111) grain boundary planes are the most numerous and have the lowest energy and (100) planes have the highest energy and are least frequent. Also, the coherent twin is the most frequently occurring boundary and lowest energy boundary. There is also an interesting similarity in the energy anisotropy for the $\Sigma 9$ boundary. In both cases, asymmetric (-111)/(1-15) tilt boundaries have the minimum energy. While this same asymmetric boundary is the most frequently observed $\Sigma 9$ in pure Ni, IN100 prefers the symmetric (1-14) boundary. IN100 also has many fewer $\Sigma 9$ boundaries than the pure Ni.

The difference in the population of $\Sigma 9$ boundaries may stem from the configuration of the $\Sigma 3$ grain boundaries. When two $\Sigma 3$ boundaries that do not share a common misorientation axis meet at a triple junction, the third boundary must be $\Sigma 9$. In the pure Ni sample, 29% of the boundaries (by number) were $\Sigma 3$ and 8.8 % were $\Sigma 9$. In IN100, $\Sigma 3$ boundaries make up 14% of the population by number and $\Sigma 9$ make up 2%. This suggests that not as many of the $\Sigma 3$ boundaries in IN100 intersect. A search of the triple junctions indicates that this is true: only 17 % of the $\Sigma 9$ boundaries meet at two $\Sigma 3$ boundaries whereas in the pure Ni 64% of the $\Sigma 9$ boundaries meet at two $\Sigma 3$ boundaries.

The trend in the data that the grain boundary energy distribution is inversely related to the grain boundary character distribution is similar to that found previously in other measurements [20,21,28] and in simulations [32-36]. A model has recently been proposed to explain the existence of a steady state grain boundary character distribution that is inversely related to the grain boundary energy distribution [37,38]. The model is based on the experimental observation that during grain growth, higher energy boundaries are more likely to be decreasing in area and lower energy boundaries are more likely to be increasing in area [38]. Based on this, if one assumes that the rate at which grain boundaries are eliminated from the system during critical events is proportional to the grain boundary energy, then steady state distributions with an inverse correlation are produced [37]. However, it should be noted that these conclusions apply only to cases in which the polycrystal is relatively untextured, evolves by normal grain growth, has reached a scale invariant structure, and does not have intergranular films or other second phases that affect grain boundary motion. When this is not the case, there are mechanisms that can sustain high mobility grain boundaries, even after they grow past an immediate neighbor and are annihilated.

Conclusions

The distribution of grain boundary planes can be accurately determined from three-dimensional EBSD data. The important factors are the alignment of the parallel layers, the ratio of the vertical to horizontal spacing, and the discretization of the domain of grain boundary types. The grain boundary plane distribution of an IN100 Ni-base super alloy shows that, in general, grain boundaries are more likely to be terminated by (111) planes than other orientations. Based on the triple junction geometry, grain boundaries terminated by (111) planes have lower energies than others. On average, the relative areas of different types of grain boundaries are inversely correlated to the relative grain boundary energies.

Acknowledgement

This work was supported at Carnegie Mellon by the MRSEC program of the National Science Foundation under Award Number DMR-0520425.

References

- [1] V. Randle and H. Davies, "A Comparison Between Three-Dimensional and Two-Dimensional Grain Boundary Plane Analysis," *Ultramicroscopy* **90** [2-3] 153-162 (2001).
- [2] D.M. Saylor, A. Morawiec, and G.S. Rohrer, "Distribution of Grain boundaries in Magnesia as a Function of Five Macroscopic Parameters," *Acta Mater.*, **51** (2003) 3663-74.
- [3] D.M. Saylor, B.S. El-Dasher, T. Sano, and G.S. Rohrer, "Distribution of Grain boundaries in SrTiO₃ as a Function of Five Macroscopic Parameters," *J. Amer. Ceram. Soc.*, **87** (2004) 670-676.
- [4] D. J. Rowenhorst, and P.W. Voorhees, "Measurements of Grain Boundary Energy and Anisotropy in Tin," *Metallurgical and Materials Transactions A* **36A** 2127-2135 (2005).
- [5] Rowenhorst DJ, Gupta A, Feng CR, Spanos G. 2006. 3D crystallographic and morphological analysis of coarse martensite: Combining EBSD and serial sectioning. *Scripta mater.* 55:11-6
- [6] D.M. Saylor, B.S. El-Dasher, B.L. Adams, and G.S. Rohrer, "Measuring the Five Parameter Grain Boundary Distribution From Observations of Planar Sections," *Metallurgical and Materials Transactions*, **35A** (2004) 1981-1989.
- [7] D.M. Saylor, B.S. El Dasher, A.D. Rollett, and G.S. Rohrer, "Distribution of Grain Boundaries in Aluminum as a Function of Five Macroscopic Parameters," *Acta Materialia*, **52** (2004) 3649-3655.
- [8] D.M. Saylor, B.S. El-Dasher, Y. Pang, H.M. Miller, P. Wynblatt, A.D. Rollett, and G.S. Rohrer, "Habits of Grains in Dense Polycrystalline Solids," *J. Amer. Ceram. Soc.*, **87** (2004) 724-726.
- [9] G.S. Rohrer, V. Randle, C.-S. Kim, and Y. Hu, "Changes in the five- parameter grain boundary character distribution in alpha-brass brought about by grain boundary engineering," *Acta Materialia* **54** (2006) 4389-4502.

- [10] S.T. Downey, II, N. Bembridge, P.N. Kalu, H.M. Miller, G.S. Rohrer, K. Han, "Grain Boundary Plane Distributions in Modified 316 LN Steel Exposed at Elevated and Cryogenic Temperatures," *J. Mater. Sci.*, 42 (2007) 9543-47.
- [11] C.-S. Kim, T.R. Massa, G.S. Rohrer, "Interface character distributions in WC-Co composites," *J. Am. Ceram. Soc.*, 91 (2007) 996-1001.
- [12] V. Randle, G.S. Rohrer, H.M. Miller, M. Coleman, G.T. Owen, "Five-parameter grain boundary distribution of commercially grain boundary engineered nickel and copper," *Acta Materialia*, 56 (2008) 2363-2373.
- [13] V. Randle, G.S. Rohrer, and Y Hu, "Five-parameter grain boundary analysis of a titanium alloy before and after low temperature annealing," *Scripta Materialia*, 58 (2008) 183-186.
- [14] M.D. Uchic, M.A. Groeber, D.M. Dimiduka, J.P. Simmons, "3D microstructural characterization of nickel superalloys via serial-sectioning using a dual beam FIB-SEM," *Scripta Materialia*, 2006. 55(1): p. 23-28.
- [15] M.A. Groeber, B.K. Haley, M.D. Uchic, D.M. Dimiduk, S. Ghosh, "3D reconstruction and characterization of polycrystalline microstructures using a FIB-SEM system," *Materials Characterization* 57 [4-5] (2006) 259-273.
- [16] Konrad, J., S. Zaefferer, and D. Raabe, "Investigation of orientation gradients around a hard Laves particle in a warm-rolled Fe₃Al-based alloy using a 3D EBSD-FIB technique," *Acta Materialia*, 2006. 54(5): p. 1369-1380.
- [17] A.C. Lewis, K.A. Jordan, A.B. Geltmacher, "Determination of the Critical Microstructural Features in an Austenitic Stainless Steel Using Image-Based Finite Element Modeling," *Metall. Mater. Trans. A* 39 [5] (2008) 1109-1117.
- [18] M. Groeber, S. Ghosh, M.D. Uchic, D.M. Dimiduk, "A framework for automated analysis and simulation of 3D polycrystalline microstructures. Part 1: Statistical characterization," *Acta Materialia* 56 (2008) 1257-1273.
- [19] M. Groeber, S. Ghosh, M.D. Uchic, D.M. Dimiduk, "A framework for automated analysis and simulation of 3D polycrystalline microstructures. Part 2: Synthetic structure generation," *Acta Materialia* 56 (2008) 1274-1287.

- [20] S.J. Dillon and G.S. Rohrer, "Characterization of the Grain Boundary Character and Energy Distributions of Yttria using Automated Serial Sectioning and EBSD in the FIB," Journal of the American Ceramic Society, (2009), in press.
- [21] J. Li, S.J. Dillon, G.S. Rohrer, (2009), *Acta Mater.*, submitted.
- [22] A.D. Rollett, S.-B. Lee, R. Campman, and G.S. Rohrer, "Three- Dimensional Characterization of Microstructure by Electron Back-Scatter Diffraction," Annual Review of Materials Research, **37** (2007) 627- 658.
- [23] OIMTools
- [24] S.I. Wright, R.J. Larsen, "Extracting Twins from Orientation Imaging Scan Data," *J. Micro.*, **205**(3), 245-52, (2002).
- [25] G.S. Rohrer, D.M. Saylor, B.S. El-Dasher, B.L. Adams, A.D. Rollett, and P. Wynblatt, "The Distribution of Internal Interfaces in Polycrystals," *Zeit.fur Metall.*, **95**, 197-214, (2004).
- [26] A. Morawiec, "Method to Calculate the Grain Boundary Energy Distribution over the Space of Macroscopic Boundary Parameters from the Geometry of Triple Junctions," *Acta Materialia*, **48**[13] 3525-3532(2000).
- [27] C. Herring, "Surface Tension as a Motivation for Sintering," 143–79, in *The Physics of Powder Metallurgy*. Edited by W. E. Kingston. McGraw-Hill, New York, (1951).
- [28] D.M. Saylor, A. Morawiec, and G.S. Rohrer, "The Relative Free Energies of Grain boundaries in Magnesia as a Function of Five Macroscopic Parameters," Acta Mater., **51** (2003) 3675-86.
- [29] Hoffman DW, Cahn JW. , "A vector thermodynamics for anisotropic surfaces. I. fundamentals and applications to plane surface junctions," *Surface Science* 1972;31:368
- [30] Cahn JW, Hoffman DW., "A vector thermodynamics for anisotropic surfaces. II. curved and faceted surfaces," *Acta Met.* 1974;22:1205
- [31] D.G. Brandon, "The Structure of High-Angle Grain Boundaries," *Acta Metall*, **14**, 1479, (1966).
- [32] E.A. Holm, G.N. Hassold, and M.A. Miodownik, "On Misorientation Distribution Evolution During Anisotropic grain Growth," *Acta Mater.*, **49**, 2981-91 (2001).

- [33] M. Upmanyu, G.N. Hassold, A. Kazaryan, E.A. Holm, Y. Wang, B. Patton, D.J. Srolovitz, "Boundary Mobility and Energy Anisotropy Effects on Microstructural Evolution During Grain Growth," *Interface Science* **10**, 201-16 (2002).
- [34] A. Kazaryan, Y. Wang, S.A. Dregia, and B.R. Patton, "Grain Growth in anisotropic systems: comparison of effects of energy and mobility," *Acta Mater.* **50** 2491-2502 (2002).
- [35] D. Kinderlehrer, I. Livshits, G.S. Rohrer, S. Ta'asan, P. Yu, "Mesoscale Simulation of the Evolution of the Grain Boundary Character Distribution," *Mater. Sci. Forum* **467-470**, 1063-68 (2004).
- [36] J. Gruber, D.C. George, A.P. Kuprat, G.S. Rohrer, A.D. Rollett, "Effect of Anisotropic Grain Boundary Properties on Grain Boundary Plane Distributions During Grain Growth," *Scripta Materialia* **53**, 351-355 (2005).
- [37] G.S. Rohrer, J. Gruber, and A.D. Rollett, "A Model for the Origin of Anisotropic Grain Boundary Character Distributions in Polycrystalline Materials," in Applications of Texture Analysis, A.D. Rollett, Editor, (*Ceram. Trans.* **201**, J. Wiley & Sons, Hoboken, NJ, 2009) 343-354.
- [38] S.J. Dillon and G.S. Rohrer, "Mechanism for the development of anisotropic grain boundary character distributions during normal grain growth," *Acta Materialia* **57** (2009) 1-7.

Figure Captions

Figure 1. Three-dimensional rendering of 96 aligned layers of orientation data for the Ni-base super-alloy. The grains are assigned random colors.

Figure 2. Inverse pole figure map of one layer of the data. The grains are colored according to the orientations given in the legend. The reconstructed grain boundary line segments (black lines) are superimposed on the map.

Figure 3. Schematic illustrating the calculation of grain boundary normals. Three grain boundary line segments on layer one (\mathbf{v}_i) meet at a triple junction. Three related segments (\mathbf{v}'_i) meet on adjacent layer 2. The triple line vector (\mathbf{l}) joins the junctions from layer 1 to layer 2. By crossing it with each line segment, a grain boundary normal (\mathbf{n}) is generated.

Figure 4. The x- and y-components of 118 triple junctions between the second and third layers (blue circles). The red squares are the same data, after aligning so that the average of all of the components equals zero. The black arrow connecting one of the circles to a square illustrates the rigid shift applied to the data.

Figure 5. The x- and y-components of the shifts between all 170 layers. The black arrow in Fig. 4 is represented as one point on this plot.

Figure 6. Schematic illustration of triple line discretization. The triple lines (arrows) must connect discrete voxels (circles) on adjacent layers. As the layer spacing increases with respect to the in-plane spacing, there are more possible inclinations for the triple line.

Figure 7. Grain boundary plane distributions in the bicrystal reference frame for the $\Sigma 3$ grain boundary ($60^\circ/[111]$). The distributions are plotted on stereographic projections and the units are multiples of a random distribution (MRD). (a) Determined from stereology. (b) Determined from three-dimensional analysis with a 1:1 vertical-to-horizontal ratio and no secondary alignment. (c) Determined from three-dimensional analysis with a 2:1 vertical-to-horizontal ratio and secondary alignment. (d) Determined from three-dimensional analysis with a 2:1 vertical-to-horizontal ratio, secondary alignment, and 11 bins per 90° .

Figure 8. (a) Distribution of grain boundary planes in the crystal reference frame, plotted in stereographic projection. (b) Relative grain boundary energies with respect to the crystal reference frame.

Figure 9. The grain boundary energy distribution for grain boundaries with the $\Sigma 3$ misorientation. The energies are plotted on a stereographic projection, in the bicrystal reference frame, and the $[001]$ axis is vertical and in the center of the plots.

Figure 10. (a-c) Grain boundary plane distributions compared to (d-f) the grain boundary energy distributions for grain boundaries with the $\Sigma 5$ (a,c), $\Sigma 7$ (b,d), and $\Sigma 9$ (c,f) misorientations. The plots are stereographic projections, in the bicrystal reference frame, and the $[001]$ axis is vertical and in the center of the plots.

Figure 11. The average populations of all grain boundaries with energies that are within the range of ± 0.05 a.u. of the energy on the horizontal axis.

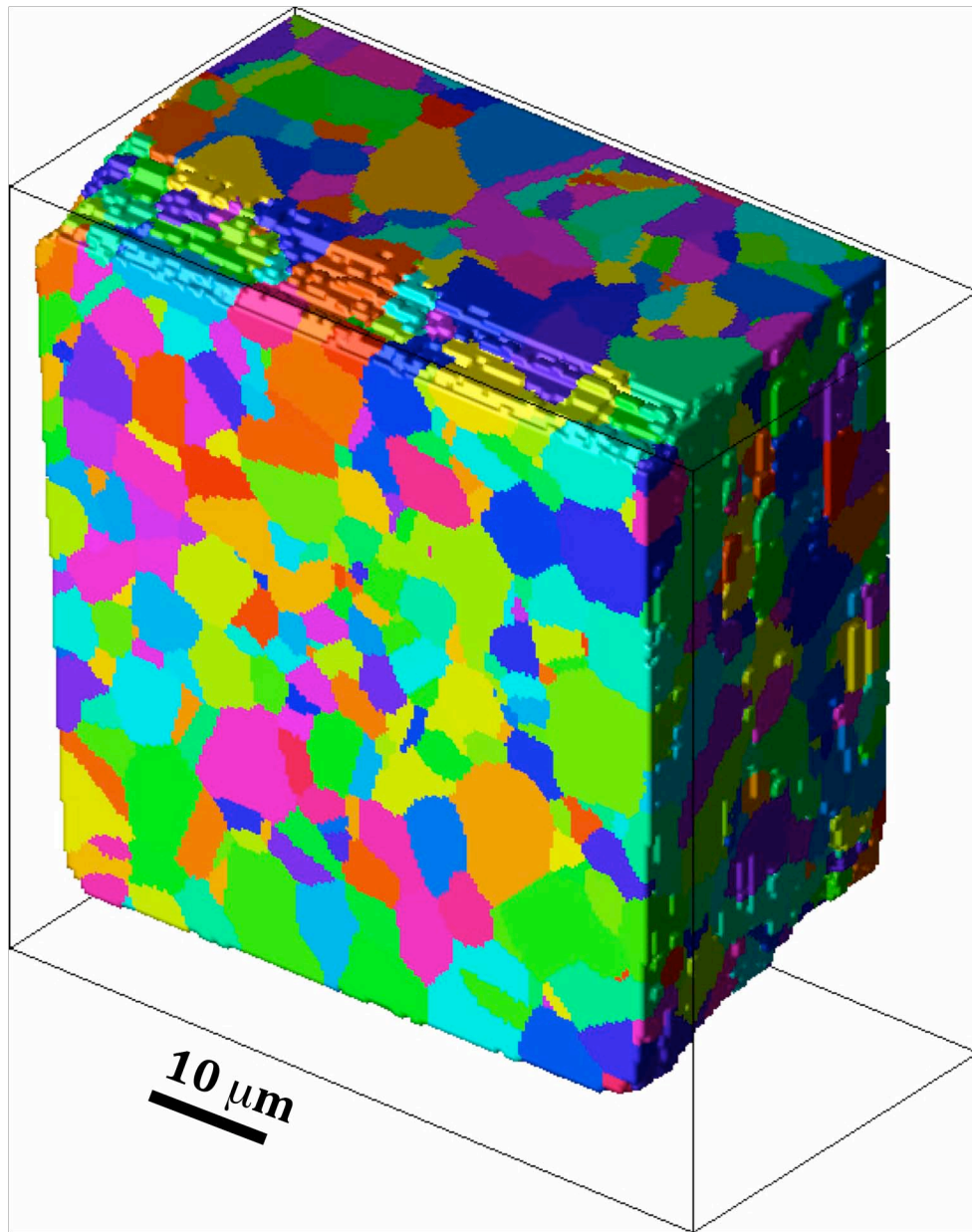


Figure 1. Three-dimensional rendering of 96 aligned layers of orientation data for the Ni-base super-alloy. The grains are assigned random colors.

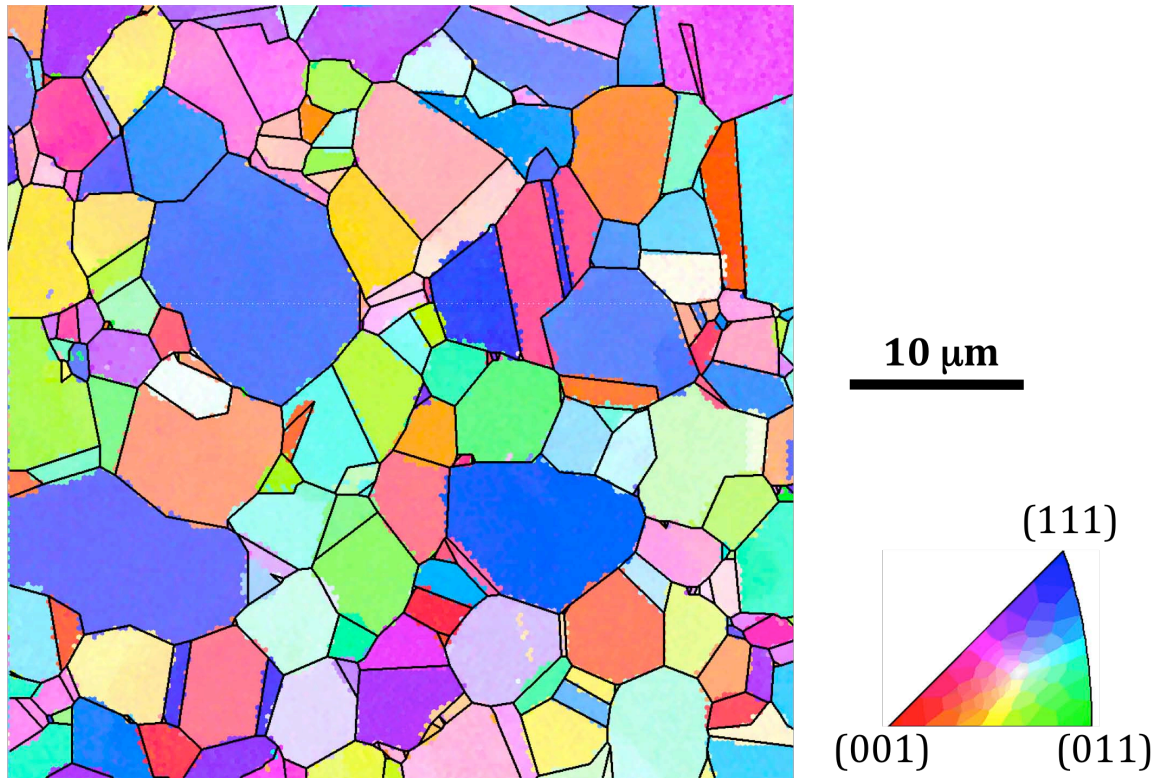


Figure 2. Inverse pole figure map of one layer of the data. The grains are colored according to the orientations given in the legend. The reconstructed grain boundary line segments (black lines) are superimposed on the map.

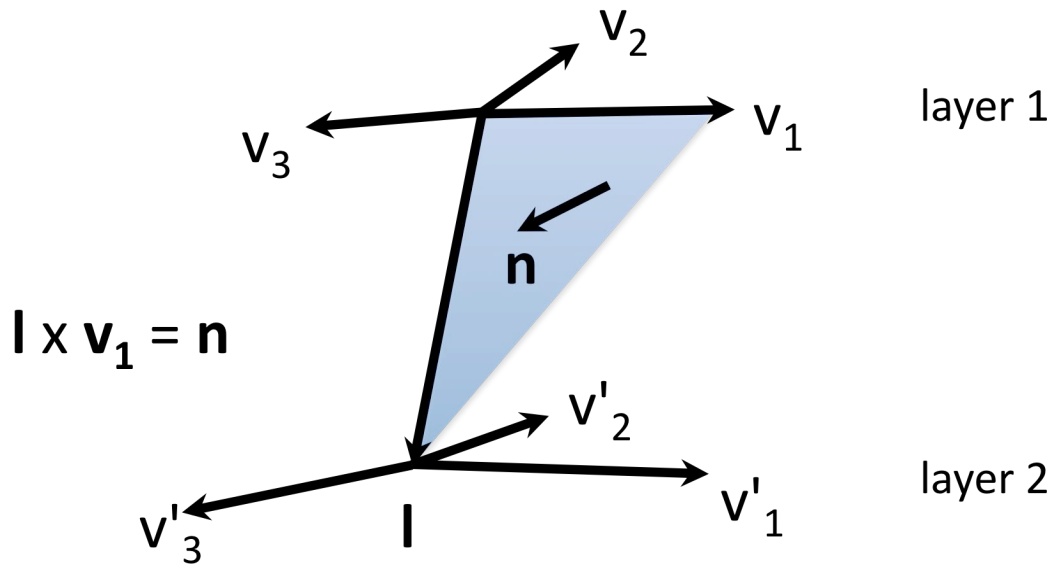


Figure 3. Schematic illustrating the calculation of grain boundary normals. Three grain boundary line segments on layer one (v_i) meet at a triple junction. Three related segments (v'_i) meet on adjacent layer 2. The triple line vector (l) joins the junctions from layer 1 to layer 2. By crossing it with each line segment, a grain boundary normal (n) is generated.

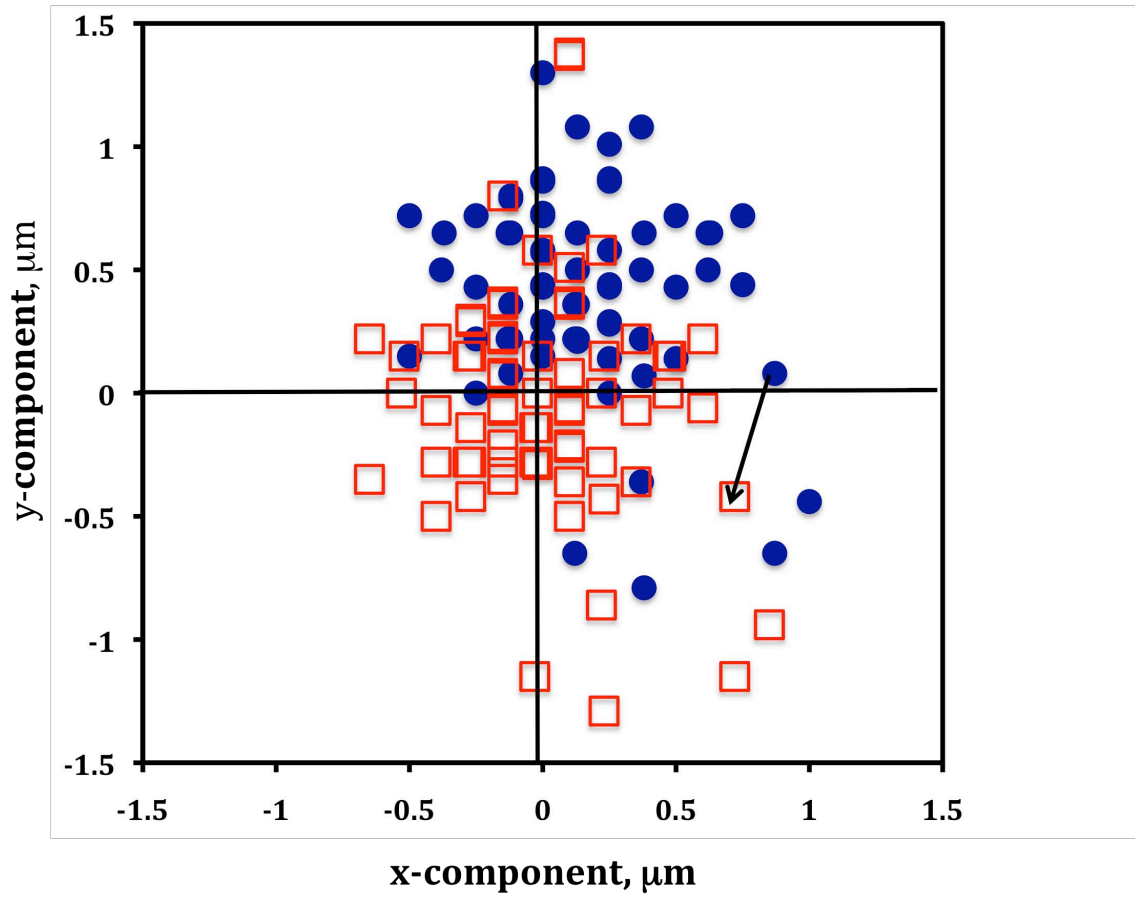


Figure 4. The x- and y-components of 118 triple junctions between the second and third layers (blue circles). The red squares are the same data, after aligning so that the average of all of the components equals zero. The black arrow connecting one of the circles to a square illustrates the rigid shift applied to the data.

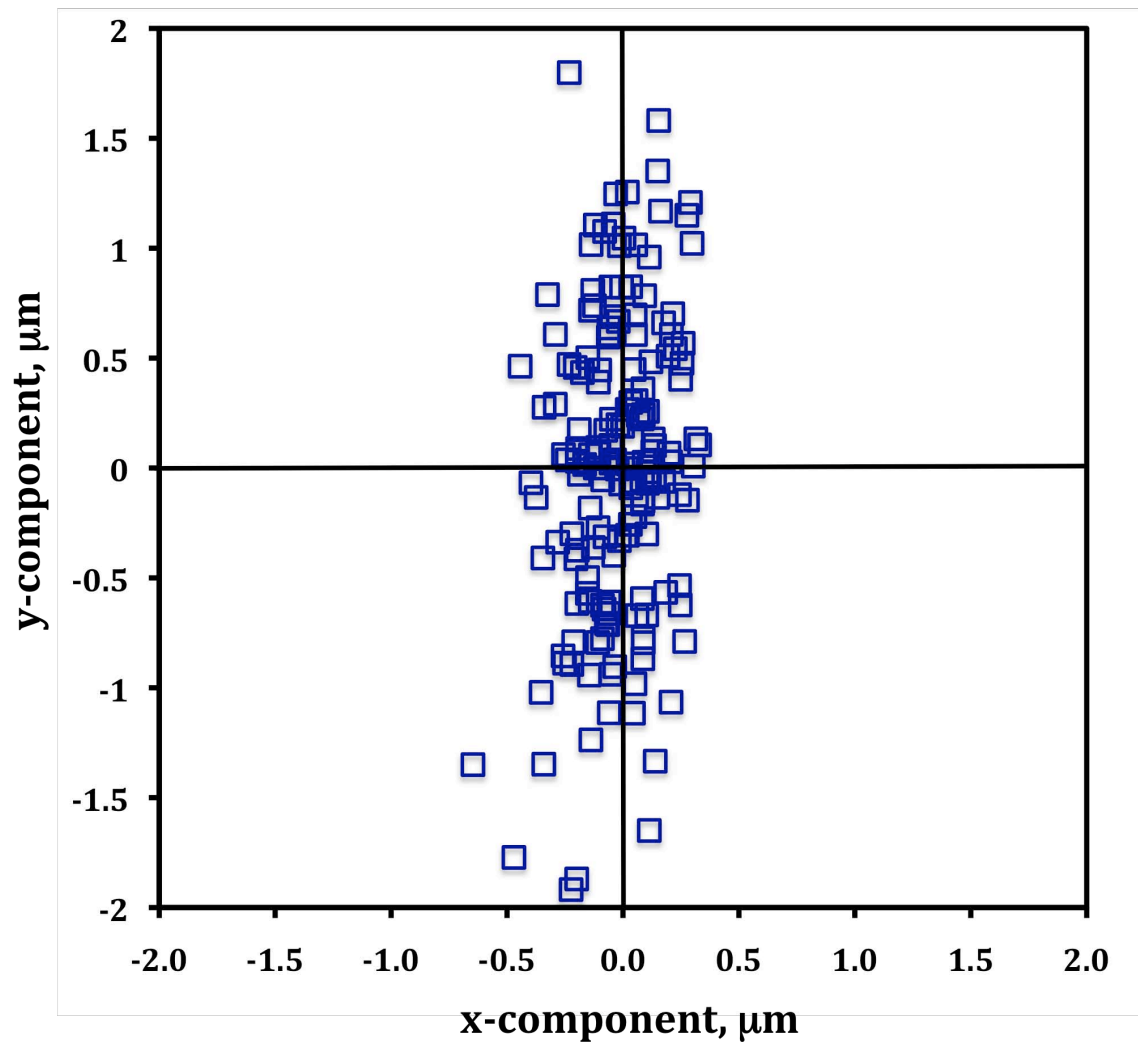


Figure 5. The x- and y-components of the shifts between all 170 layers. The black arrow in Fig. 4 is represented as one point on this plot.

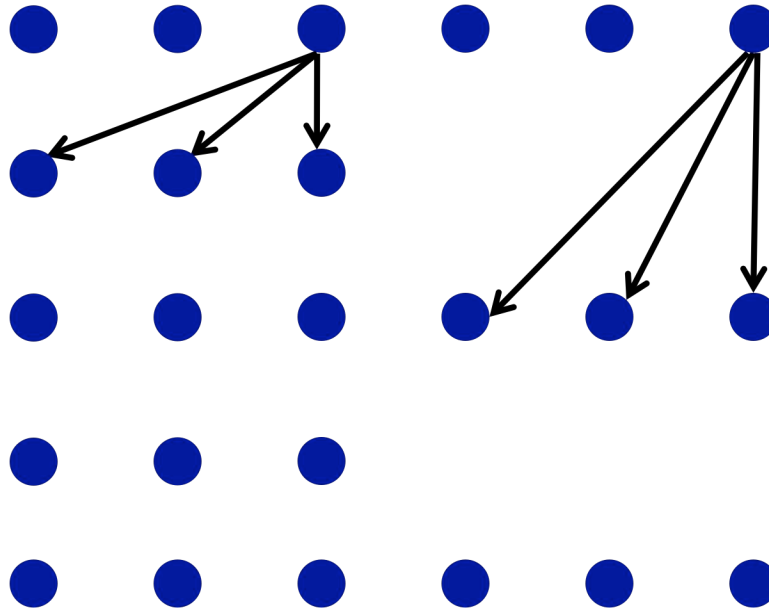


Figure 6. Schematic illustration of triple line discretization. The triple lines (arrows) must connect discrete voxels (circles) on adjacent layers. As the layer spacing increases with respect to the in-plane spacing, there are more possible inclinations for the triple line.

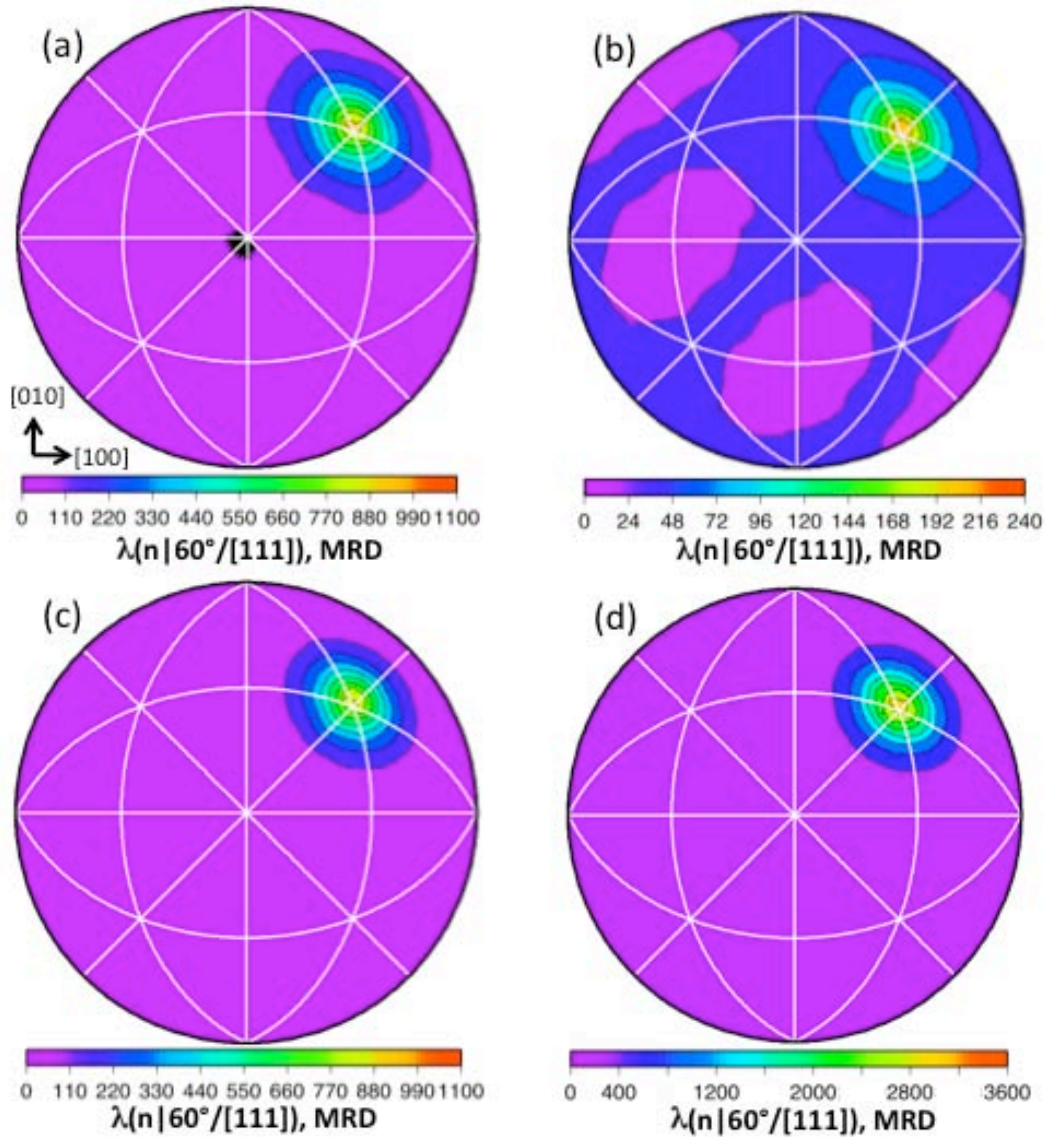


Figure 7. Grain boundary plane distributions in the bicrystal reference frame for the $\Sigma 3$ grain boundary ($60^\circ/[111]$). The distributions are plotted on stereographic projections and the units are multiples of a random distribution (MRD). (a) Determined from stereology. (b) Determined from three-dimensional analysis with a 1:1 vertical-to-horizontal ratio and no secondary alignment. (c) Determined from three-dimensional analysis with a 2:1 vertical-to-horizontal ratio and secondary alignment. (d) Determined from three-dimensional analysis with a 2:1 vertical-to-horizontal ratio, secondary alignment, and 11 bins per 90° .

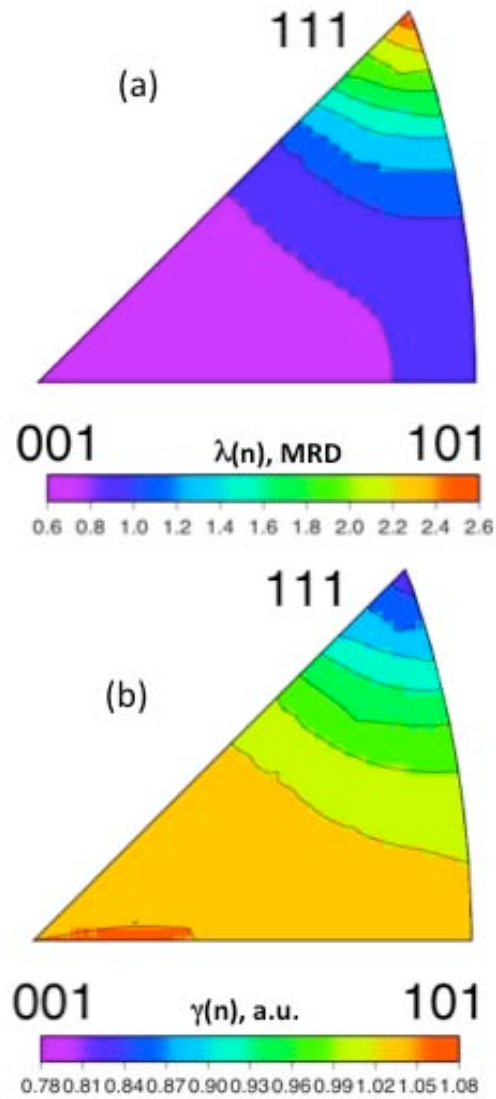


Figure 8. (a) Distribution of grain boundary planes in the crystal reference frame, plotted in stereographic projection. (b) Relative grain boundary energies with respect to the crystal reference frame.

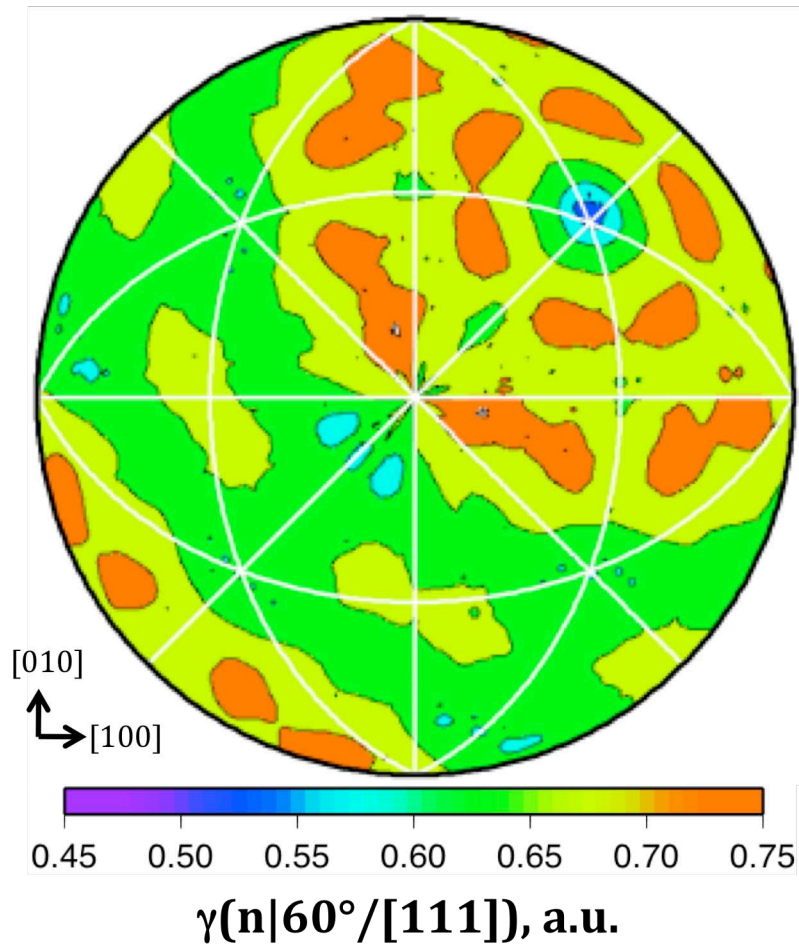


Figure 9. The grain boundary energy distribution for grain boundaries with the $\Sigma 3$ misorientation. The energies are plotted on a stereographic projection, in the bicrystal reference frame, and the $[001]$ axis is vertical and in the center of the plots.

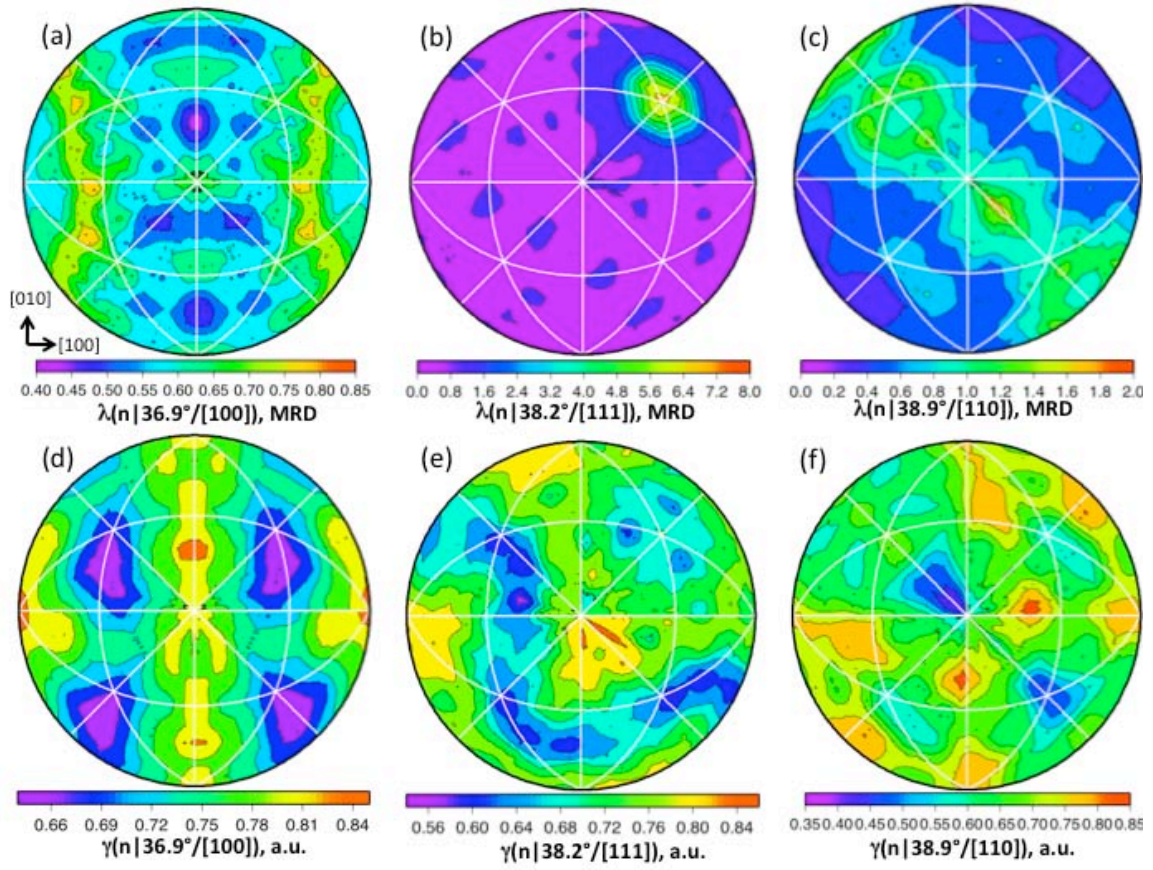


Figure 10. (a-c) Grain boundary plane distributions compared to (d-f) the grain boundary energy distributions for grain boundaries with the $\Sigma 5$ (a,c), $\Sigma 7$ (b,d), and $\Sigma 9$ (c,f) misorientations. The plots are stereographic projections, in the bicrystal reference frame, and the $[001]$ axis is vertical and in the center of the plots.

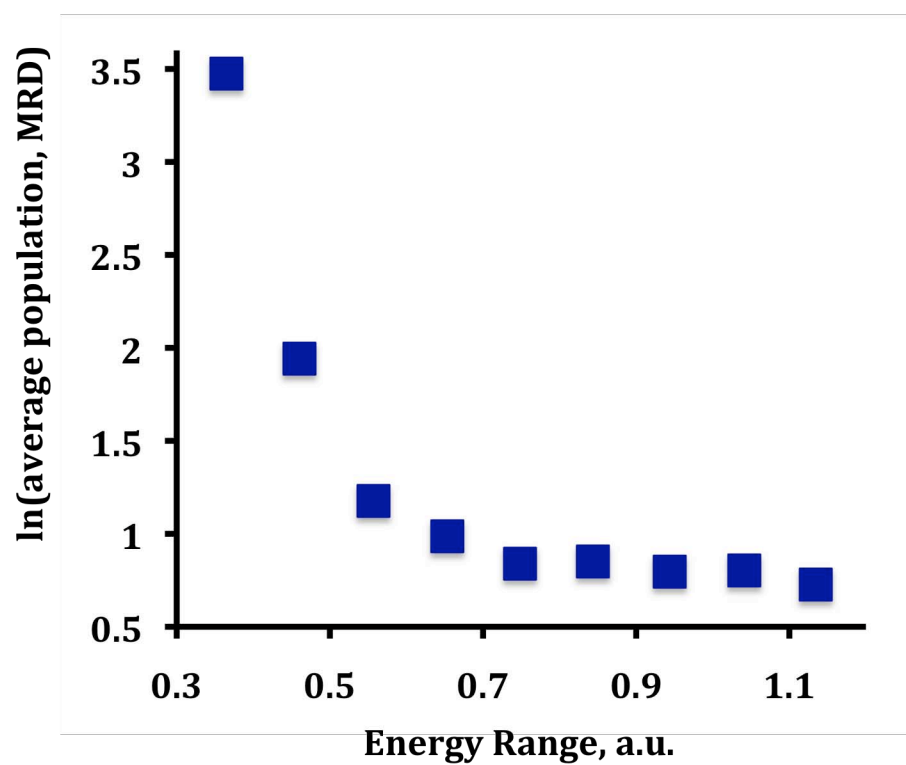


Figure 11. The average populations of all grain boundaries with energies that are within the range of ± 0.05 a.u. of the energy on the horizontal axis.